Prepared for submission to JHEP

Study of Central Exclusive Production of $\pi^+\pi^-$, K^+K^- and $p\bar{p}$ Pairs in Proton-Proton Collisions at $\sqrt{s} = 510$ GeV with the STAR Detector at RHIC

The STAR Collaboration

E-mail: Tomas.Truhlar@fjfi.cvut.cz

Abstract: We report on the first measurement of the Central Exclusive Production (CEP) process in proton-proton (pp) collisions:, $pp \rightarrow ph^+h^-p$ (where $h = \pi, K, p$) at the center-of-mass energy $\sqrt{s} = 510$ GeV with the STAR experiment at RHIC. At this energy, the process is dominated by a double $\mathbb{P}$omeron exchange mechanism. Hence, it provides a clean environment for investigating $\mathbb{P}$omeron interactions by measuring fully reconstructed final states involving only two hadrons and two forward scattered protons. The oppositely charged hadron pairs are measured within the central detector of STAR. The forward scattered protons are measured in the Roman Pot system allowing the verification of the event's exclusivity. Differential fiducial cross sections within the STAR acceptance are presented as a function of the difference in the azimuthal angle between the outgoing protons. The invariant masses of the charged hadron pairs are measured up to approximately 3 GeV and the square of the four-momentum transfer (t_1 and t_2) of the two forward-scattered protons in the range 0.3 GeV$^2 < -t_1, -t_2 < 1.6$ GeV^2. The differential fiducial cross sections of the forward protons as a function of the $|t_1 + t_2|$ are also presented. All results for the $\pi^+\pi^-$ pair are presented in three mass ranges. A comparison with GRANIITTI Monte Carlo predictions are also presented, where the spectra include continuum and resonant contributions. The observed spectra are consistent with double $\mathbb{P}$omeron exchange, including resonances seen in previous studies, while the $f_0(980)$ resonance is reported here for the first time in the K^+K^- decay channel.

Contents

1 Introduction

Measurement of CEP of charged hadron pairs in the Double $\mathbb{P}$omeron Exchange (D$\mathbb{P}$E) process [1] provides a unique opportunity to study quantum chromodynamics (QCD), the theory of strong interactions. The validity of QCD has been demonstrated in many experiments since the 1970s, in particular at hadron colliders, like the measurements of CEP in D$\mathbb{P}$E at the Intersecting Storage Rings (ISR) by the AFS [2] experiment, at RHIC by the STAR [3] experiment, and at the Large Hadron Collider (LHC) by the CMS and TOTEM [4] and ATLAS [5] experiments, and also by the measurement of central production at the Tevatron by the CDF [6] experiment. While these results confirm the validity of QCD, they also make clear that the non-perturbative regime remains insufficiently understood.

CEP in D$\mathbb{P}$E probes the non-perturbative regime of QCD where Regge theory is often used to describe such interactions. In QCD, the $\mathbb{P}$omeron is modeled as a color-singlet object. In the lowest order, it can be represented as a two-gluon exchange. As no color is exchanged in D$\mathbb{P}$E, the color content of each proton is preserved allowing both protons to stay intact after the collision. The presence of large rapidity gaps between the centrally produced system and the outgoing protons is a key signature of such events.

These features make D$\mathbb{P}$E a suitable environment for exploring the details of the $\mathbb{P}$omeron exchange and the non-perturbative aspect of QCD. However, theoretical non-perturbative approaches [7, 8] remain challenging due to the theoretical complexity of the process, which involves significant interference between resonant and continuum production, as well as re-scattering effects via additional interaction between the protons. The charged hadron pairs produced in D$\mathbb{P}$E are constrained to quantum numbers $I^G J^{PC} = 0^+(\text{even})^{++}$. This constraint acts as a "quantum number filter" making D$\mathbb{P}$E a powerful tool for meson spectroscopy, particularly for identifying gluon-rich states. In addition, such measurements provide valuable insight into the $\mathbb{P}$omeron itself [9], and absorption effects [10, 11] especially thanks to measurement of forward-scattered protons. Furthermore, the D$\mathbb{P}$E provides a gluon-rich environment suitable to study production of glueballs [12], bound states of gluons. Experimental confirmation of glueball existence would be yet another strong support for the validity of QCD. However, the exact nature of the $\mathbb{P}$omeron still remains elusive and the existence of a glueball has not been unambiguously confirmed yet.

Figure 1 shows diagrams of production h^+h^- pairs, where h^+h^- are $\pi^+\pi^-$, K^+K^-, and $p\bar{p}$, in the D$\mathbb{P}$E process, in the non-perturbative QCD regime: central exclusive resonant production (left) and continuum (non-resonant) production (middle). Representation of continuum production within perturbative QCD is shown in the two-gluon approximation model (right). There are three possible mechanism of CEP: double photon exchange, photoproduction, and D$\mathbb{P}$E. The last one is expected to be dominant CEP mechanism [13, 14] at RHIC energies.

By definition, CEP is a process where colliding protons stay intact after the collision. The outgoing intact protons are studied using detectors placed in special vessels called Roman Pots (RP) [15]. The produced hadrons, which are well separated from the forward-scattered protons by rapidity gaps, characteristic of D$\mathbb{P}$E, are produced in the center of rapidity. They are measured in the Time Projection Chamber (TPC) [16] and in the Time of Flight (TOF) systems [17]. The rapidity gaps $2.1 < |\eta| < 5.0$ are ensured by vetoes within the Beam-Beam Counters (BBC) [18] acceptance. By definition, "exclusive" means that all particles in the final state are measured. This gives us full control of the interaction's kinematics and verification of its exclusivity.

This paper presents the first measurement of $\pi^+\pi^-$, K^+K^-, and $p\bar{p}$ production in

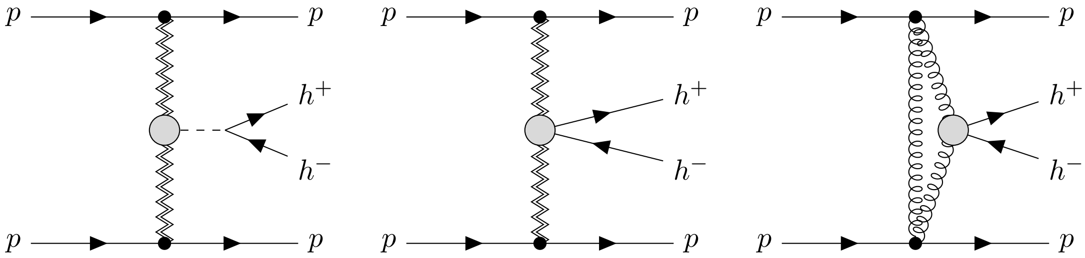

Figure 1. Diagrams of CEP of h^+h^- in the D$\mathbb{P}$E process. The resonant (left) and continuum production (middle) are shown. The two-gluon approximation of continuum production in D$\mathbb{P}$E in perturbative QCD (right) is also shown. $\mathbb{P}$omerons are represented by double zigzag lines and gluons by spiral lines.

the CEP processes in pp collisions at $\sqrt{s}$ = 510 GeV using the STAR detector at the Relativistic Heavy Ion Collider (RHIC) [19, 20].

Differential and integrated cross sections are measured within the STAR detector's acceptance. The results are compared with the previous STAR results on CEP of charged hadron pairs in pp collisions at $\sqrt{s}$ = 200 GeV [3]. Throughout the paper, the natural units $c = \hbar = 1$ are used.

2 Experimental setup

STAR is a general-purpose detector at RHIC, with a 0.5 Tesla [21] solenoidal magnetic field parallel to the beam axis. This measurement utilizes various subsystems of the STAR detector in a configuration similar to that used for the CEP measurements in proton-proton collisions at $\sqrt{s}$ = 200 GeV [3]. Figure 2 shows the STAR detector with its sub-detectors, namely TPC, TOF, BBC, the Vertex Position Detector (VPD) [22], and the Barrel Electromagnetic Calorimeter (BEMC). Furthermore, the STAR experiment includes forward systems: the Zero-Degree Calorimeters (ZDC) [23, 24] and the RP system. These sub-detectors are particularly important for the CEP analysis, especially the RP system. In the following, the sub-detectors are briefly described.

The TPC is a gas-filled detector, which provides both tracking information and an average ionization energy loss per unit length ($\langle dE/dx \rangle$) for each track. The momentum reconstruction and the $\langle dE/dx \rangle$ allow identification of charged hadrons: pions, kaons, and protons. It has a cylindrical shape with a length of 4.2 m, an inner radius of 0.5 m and an outer radius of 2 m. The TPC has full azimuthal coverage $0 < \varphi < 2\pi$, and pseudorapidity coverage $|\eta| < 1.0$ for charged particle detection and identification[1].

The TOF system is a cylindrical detector around the TPC extending the particle identification (PID) capabilities of the TPC for particles with momenta up to ~ 3 GeV. The

[1]The origin is at the interaction point (IP) at the center of the detector. The z-axis is aligned with the center of the beam pipe, the x-axis points radially outward from the IP toward the outside of the RHIC ring, and the y-axis points vertically up. The pseudorapidity η is defined in terms of the polar angle θ as $\eta = -\ln\left(\tan\left(\frac{\theta}{2}\right)\right)$.

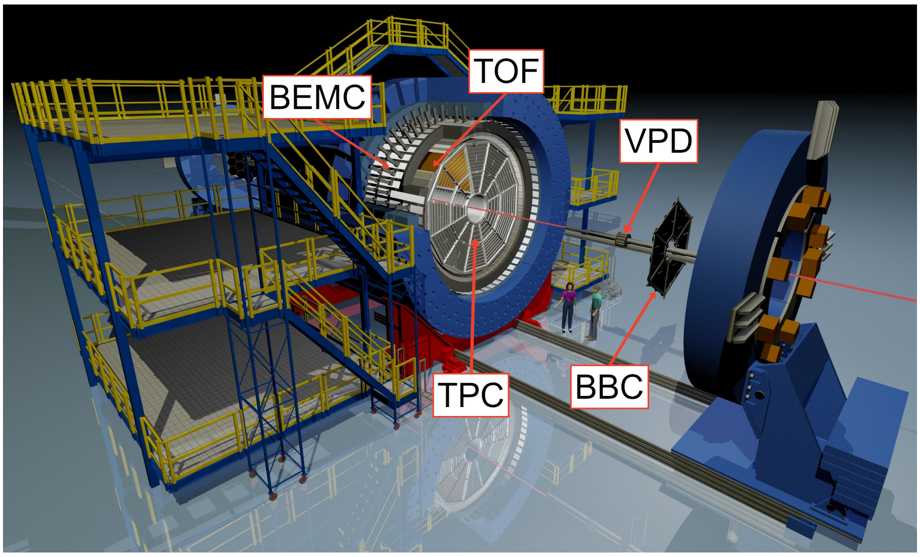

Figure 2. The schematic view of the STAR experiment. The main sub-detectors, including the TPC, the TOF, the BBC, the VPD and the BEMC are highlighted.

TOF is composed of adjacent Multi-gap Resistive Plate Chambers covering full azimuthal angle and pseudorapidity $|\eta| < 0.9$. It is a fast timing detector with a time resolution between $60 - 100$ ps. Therefore, it is often used to trigger on charged particle multiplicity in the central rapidity. For the CEP events, it is crucial for triggering on low multiplicity events in the TPC. Moreover, it helps to discriminate in-time TPC tracks from different bunch crossings (out-of-time pile-up).

The BBC is an array of plastic scintillator detectors designed to detect high$-\eta$ particles produced in the forward direction. The BBC consists of two identical detectors placed at ± 3.74 m from the IP. Each detector is formed by 36 hexagonal scintillator tiles, covering a pseudorapidity range of $2.1 < |\eta| < 3.3$, and 18 large tiles covering $3.3 < |\eta| < 5.0$, respectively. For the CEP events, it is used as a rapidity gap veto, to ensure the rapidity gaps between the central produced system and forward-scattered protons.

The ZDC's main function is to measure neutral particles produced in the forward direction, $\theta \lesssim 4$ mrad. They are placed on each side of the IP at a distance of ± 18 m, directly in line with the STAR beam pipe behind the DX dipole magnets. These magnets deflect charged particles, including the forward protons. They are used to detect beam energy neutrons produced in the forward direction close to the beam direction. Both BBC and ZDC are used to ensure a rapidity gap within their acceptance, thereby reducing background due to the non-exclusive events at the trigger level.

The RPs are used to detect and measure forward protons scattered at very small angles (few mrad), whose trajectories are contained in the accelerator beam pipe. For that purpose, the STAR experiment was upgraded with the RP system previously used by the PP2PP experiment [15]. Two RP stations were installed on each side of the IP at a distance of ± 15.8 m and ± 17.6 m from the IP. The location of the RPs, top and side views, and the coordinate system are shown schematically in figure 3. Each RP station has two movable RP vessels: one above and one below the beam pipe. Each stainless steel RP vessel houses a Silicon Strip Detector (SSD) package and a scintillation counter. The SSD package consists of four SSDs measuring proton position in the $x-y$ plane, two measuring $x-$coordinate and two measuring $y-$coordinate. The detector package has transverse size 5×8 cm^2 and a depth 3.5 cm. The silicon sensor is 400 μm thick, while the trigger scintillator is 5 mm thick. The strips in the silicon detectors are approximately 100 μm wide. The typical distance of the first horizontal strip from the beam is about 2 cm. Having two RP stations on each side allows momentum reconstruction of scattered protons. The scintillation counter was used to trigger on forward protons. Each trigger counter was read out by two photomultipliers. The stainless steel vessel separates the detector package from the machine vacuum allowing operation of the package at normal atmospheric pressure.

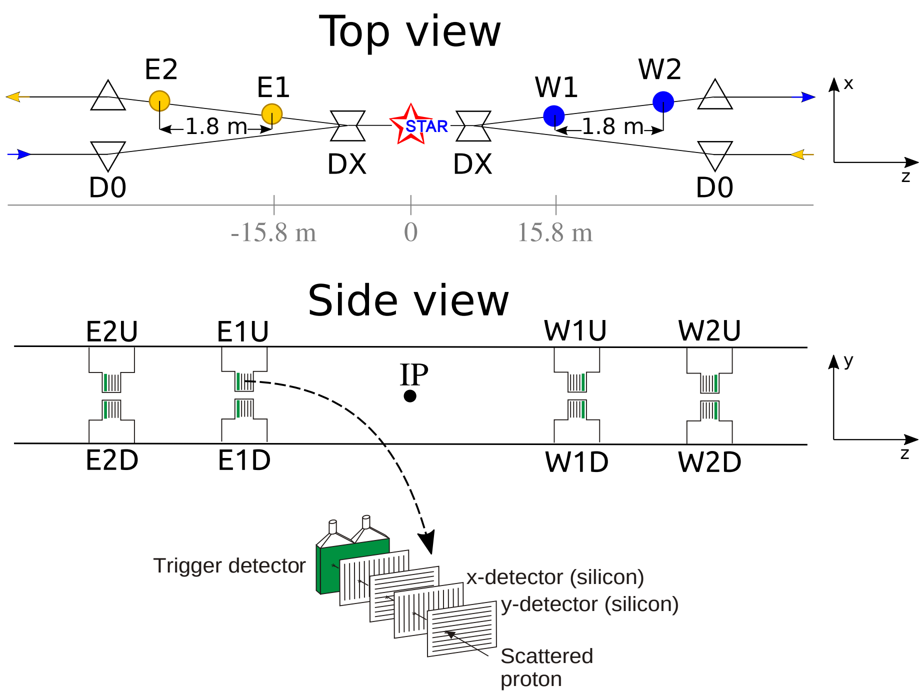

Figure 3. The layout of the RP setup at STAR (not to scale) for measuring forward protons. Top (x, z) and side (y, z) views are shown. Two sets of RPs, labeled (W1, W2) and (E1, E2) were installed between the DX and D0 magnets, at ±15.8 m and ±17.6 m, on either side of the IP. The detector package has transverse size 5×8 cm^2 and a depth 3.5 cm. The silicon sensor is 400 μm thick, while the trigger scintillator is 5 mm thick. The strips in the silicon detectors are ≈ 100 μm wide. Two dipole magnets, DX and D0, which bend the beams into and out of the IP, are also shown. The top view shows highlighted Roman Pot stations E1, E2, W1, W2 and dipole magnets DX, D0. The side view depicts Roman Pots. Taken from Ref. [25].

There is an RP naming convention that denotes the position of each RP. The RP names are in the following format: side of the IP (E or W), station (1 or 2), and orientation (U or D). For example, the first RP, as measured away from the IP, located on the west side of the IP above the beam line, is called W1U. Moreover, the RP system is divided into four branches (EU, ED, WU, and WD), in which proton tracks can be reconstructed. A branch is composed of two RP on the same side of the IP (E or W) and with the same orientation (U or D). For example, the EU branch is composed of E1U and E2U RPs.

The RP stations are placed behind the DX magnet, the RHIC-lattice dipole magnet closest to the IP. This positioning allows the measurement of the momentum vector of the scattered protons at the detection point. The symmetry of the RHIC rings requires that the magnetic fields in the DX magnets are the same, and the relative differences of DX magnet strengths are at the 10^{-3} level [26]. The RP layout ensures that no special beam conditions are needed to operate the RP detectors.

After the RP installation, a survey was performed to determine the position in space of the first strip in each detector package in the STAR coordinate system, the so-called baseline survey alignment. Corrections to the baseline survey alignment were obtained using elastically scattered protons. The collinearity constraint was applied, which required that the two reconstructed tracks on each side of the IP lie on the same straight line. The alignment method is the same as described in Ref. [25] and used in Refs. [3, 25, 26]. The obtained corrections are applied to correct the position of reconstructed points. The average final correction over all runs is 20 ± 10 μm, consistent with the one obtained in Ref. [26].

3 Triggers

The trigger for CEP events was based on the topology of those events. The following trigger conditions were required:

1. At least one proton on each side of the IP. An energy deposit consistent with a minimum ionizing particle (MIP) in time with the beam crossing, was required in exactly one branch on each side of the IP. A veto was imposed on the other branches to reject either proton dissociation or pile-up events. This signal ensures the presence of at least two forward-scattered protons.

2. At least two charged particles in central rapidity. This was implemented by requiring the TOF multiplicity ≥ 2. The upper limit on the TOF multiplicity (≤ 10) was applied to reject high multiplicity events. This allowed good acceptance for four-pion events and avoided rejection of CEP events which could overlap with a small level of noise.

3. A rapidity gap between the central system and forward protons. A veto on a signal consistent with a minimum ionizing particle in small or large BBC tiles, or an energy deposition in the ZDCs above a few tens of GeV on either side of the IP was used to ensure the double-gap topology typical of CEP events.

4 Event selection

Three primary sets of selection criteria are implemented to select CEP events: 1) selection of forward protons; 2) selection of tracks in the TPC: particle identification associated with the tracks and fiducial acceptance of the tracks in the TPC; 3) exclusivity cut using balance of transverse momentum (p_T) of all measured particles, ($p_\mathrm{T}^\mathrm{miss}$). The cuts are chosen to ensure high signal to noise ratio and efficiency. They are explained in more detail in the following sections.

4.1 RP tracks

In order to reconstruct the position and momentum of the forward protons, we follow the approach from Refs. [3, 25, 26]. First, space points are reconstructed in each RP. Second, events with only one space point per RP are used to reconstruct a track. For these events, the transverse momentum of the protons (p_x, p_y) is reconstructed based on the positions of space points assuming a constant and uniform magnetic field inside the DX magnet. To select CEP event candidates, exactly one RP track on each side of the IP is required. Each track must have at least three out of four SSD planes used in its space point reconstruction in each RP. Furthermore, to ensure high acceptance, RP efficiency, and low systematic uncertainties, the reconstructed protons have to have momenta (p_x, p_y) inside a fiducial volume, shown in figure 4 and defined by an "and" of the following conditions (4.1):

$$\begin{aligned}
&|p_y| > p_y^\mathrm{min} \wedge p_x > p_x^\mathrm{min} \\
&(p_x + p_x^\mathrm{center})^2 + p_y^2 < R^2 \\
&(p_y > 0 \quad \text{for EU and WU}) \wedge (p_y < 0 \quad \text{for ED and WD}) \\
&|p_y| < p_y^\mathrm{max} \quad \text{for EU and WD} \\
&(p_x + \bar{p}_x^\mathrm{center})^2 + p_y^2 < \bar{R}^2 \quad \text{for ED and WU},
\end{aligned} \tag{4.1}$$

where the parameters (p_y^min, p_x^min, p_x^center, R^2, p_y^max, $\bar{p}_x^\mathrm{center}$, and $\bar{R}^2$) describe the acceptance of the protons in the RPs and are summarized in table 1. The parameters R and $\bar{R}$ define the circles in the acceptance plots in the (p_x, p_y) momentum space.

	EU	ED	WU	WD
p_x^min (GeV)	-0.23	-0.25	-0.21	-0.19
p_y^min (GeV)	0.42	0.48	0.46	0.46
p_y^max (GeV)	0.86	0.84	0.84	0.88
p_x^center (GeV)	0.64	0.7	0.6	0.7
R^2 (GeV^2)	1.36	1.5	1.3	1.5
$\bar{p}_x^\mathrm{center}$ (GeV)	0.0	-0.25	-0.28	0.0
p_x^max (GeV)	0.0	0.06	0.03	0.0
$\bar{R}^2$ (GeV^2)	0.0	0.959	0.946	0.0

Table 1. The summary of parameters defining the fiducial volume.

Since the cross section drops with increasing scattering angle (i.e. increasing $|p_y|$), most of the scattered protons are at low $|p_y|$. However, the probability of measuring a proton from the beam halo[2] increases as the RPs get closer to the beam axis (decreasing

[2]The beam halo consists of particles traveling with the main beam, most of which are protons. These

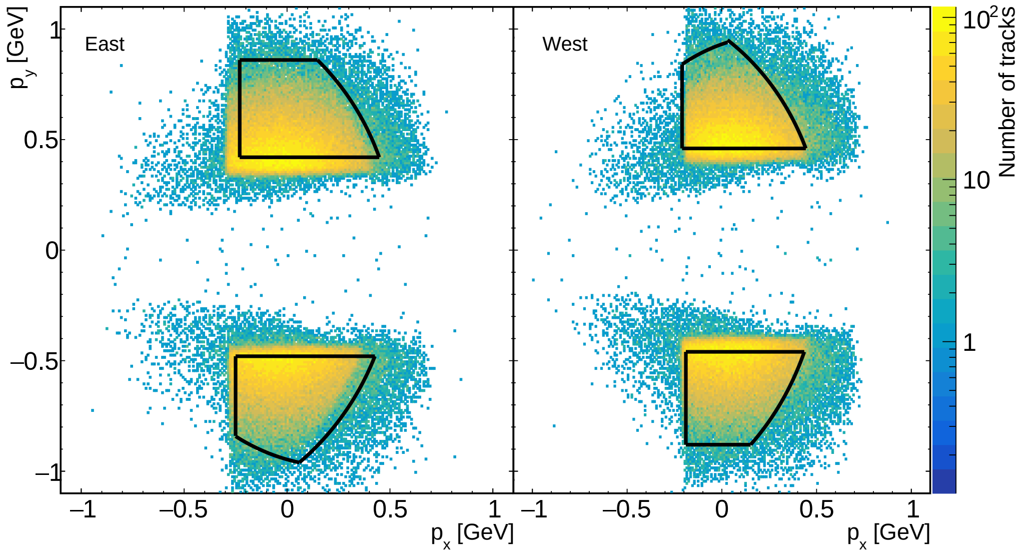

Figure 4. The RP fiducial volume shown with black solid lines on top of the combined distributions of forward protons' momenta p_y vs. p_x reconstructed with the East and West RP stations.

$|p_y|$). In order to maximize the acceptance, it is necessary to get $|p_y|$ as low as possible for each branch separately. Hence, the chosen fiducial volume optimizes acceptance and signal to noise ratio.

4.2 Primary vertex

In order to reject events with more than one inelastic interaction per bunch crossing, exactly one primary vertex is required in each event. In addition, the vertex must be reconstructed within ± 100 cm from the IP along the $z-$axis to assure optimized event acceptance.

4.3 TPC tracks

In order to select tracks in time with the bunch crossing and to extend the momentum range in which efficient PID can be provided for the central state, only tracks matching valid TOF hits are used. Therefore, tracks are required to have $p_{\mathrm{T}} > 250$ MeV, where the TPC acceptance is high and uniform. This also ensures that the track can reach the TOF detector. Track quality criteria are imposed to achieve good momentum and energy loss resolution. Namely, a minimum of 20 hits in the TPC are required for the track reconstruction ($N_{\mathrm{hits}}^{\mathrm{fit}} \geq 20$) out of which a minimum of 15 hits are required to calculate $\langle dE/dx \rangle$ ($N_{\mathrm{hits}}^{\langle dE/dx \rangle} \geq 15$). In addition to the above, only tracks with a good match to the primary vertex are further analyzed. A track has a good match to a vertex if its distance of closest approach (DCA) to the vertex in the transverse plane (DCA_{xy}) is smaller than 1.5 cm and in the z-direction (DCA_z) is smaller than 1.0 cm.

---

particles are typically located at transverse distances greater than 10σ of the beam size from the beam center.

To select CEP event candidates, only events with exactly two tracks satisfying the above criteria and with opposite charge are considered. To ensure high geometric acceptance and efficiency, the tracks are further required to have pseudorapidity within the fiducial acceptance defined by (4.2):

$$(-\frac{1}{250\ [\text{cm}]} z_{\text{vtx}} - 0.9 < \eta < -\frac{1}{250\ [\text{cm}]} z_{\text{vtx}} + 0.9) \wedge (|\eta| < 0.9), \tag{4.2}$$

where η is the track's pseudorapidity and z_{vtx} is the z-position of the primary vertex in centimeters. The equation takes into account the change of the acceptance in pseudorapidity as a function of the z-position of the primary vertex.

4.4 Exclusivity cut

Finally, an exclusivity requirement is imposed to select CEP event candidates. The detection and reconstruction of forward-scattered protons in the RP detectors, together with the central system, allow the calculation of the missing transverse momentum, defined as the sum of the transverse momenta of all measured particles:

$$p_{\mathsf{T}}^{\text{miss}} := |\, (\vec{p}_p + \vec{p}_{h^+} + \vec{p}_{h^-} + \vec{p}_p)_{\mathsf{T}}\,|. \tag{4.3}$$

In the CEP processes, the $p_{\mathsf{T}}^{\text{miss}}$ should be equal to zero due to momentum conservation. The distribution of $p_{\mathsf{T}}^{\text{miss}}$ of the events passing the first two set of criteria is shown in figure 5. The peak at low $p_{\mathsf{T}}^{\text{miss}}$ is due to the exclusive events. In each coordinate in the $(p_x^{\text{miss}}, p_y^{\text{miss}})$ space, the peaks are centered at zero. However, in any event the $(p_x^{\text{miss}}, p_y^{\text{miss}})$ do not have to be zero at the same time, hence the peak in the $p_{\mathsf{T}}^{\text{miss}}$ is shifted. Its width is predominantly determined by the beam angular divergence of 90 μrad. Events are selected if they have $p_{\mathsf{T}}^{\text{miss}} < 120$ MeV as illustrated by the black dashed line in figure 5. The red line is the fit and its extrapolation into the signal region.

4.5 Particle identification

The PID is based on combined information from the TPC, particle's $\langle dE/dx \rangle$, and its time of flight in the TOF detector. The combined information is used to identify hadron pairs: $\pi^+\pi^-, K^+K^-,$ or $p\bar{p}$. For this purpose, the χ^2 of the pair hypothesis is defined as:

$$\chi^2_{\langle dE/dx \rangle}(h^+h^-) = (n\sigma_{h^+})^2 + (n\sigma_{h^-})^2\,, \tag{4.4}$$

where $n\sigma_h$ is the number of standard deviations between the measured and the expected energy loss [27] for a given hadron. Figure 6 (left) shows the log of the $\langle dE/dx \rangle$ of charged particles as a function of the log of their momentum. Pions, kaons, and protons are clearly seen.

To extend the PID capabilities of the $\langle dE/dx \rangle$ method, the TOF information is used. However, the standard method based on the inverse particle velocity $(1/\beta)$ cannot be used for CEP events. This is due to lack of the starting time of the collision, which is reconstructed from a signal in the VPD detectors. Instead, the difference in particle time of flight can be used for identifying particle pairs without an explicitly measured starting

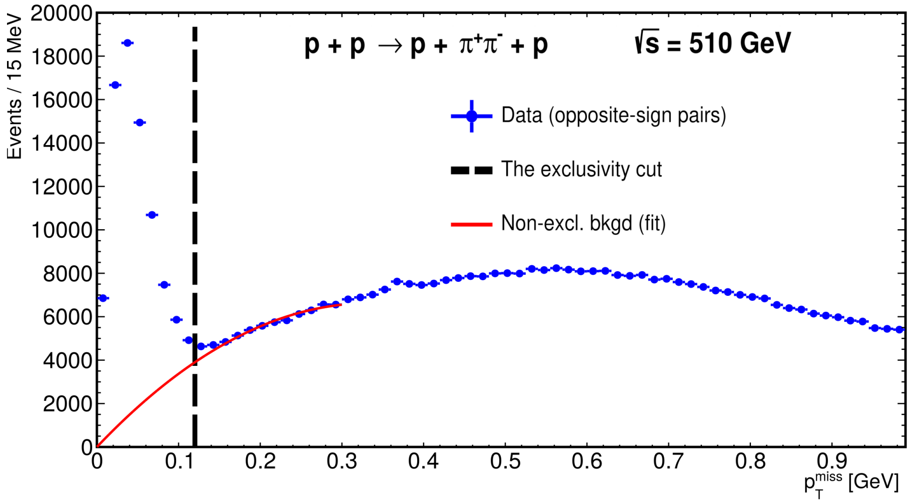

Figure 5. The distribution $p_{\mathrm{T}}^{\mathrm{miss}}$ for $\pi^+\pi^-$ CEP event candidates with the $p_{\mathrm{T}}^{\mathrm{miss}}$ cut illustrated by the black dashed line. The non-exclusive background is fitted using a second-degree polynomial with the constant term set to zero. The fit is depicted by the red line and projected into the signal region.

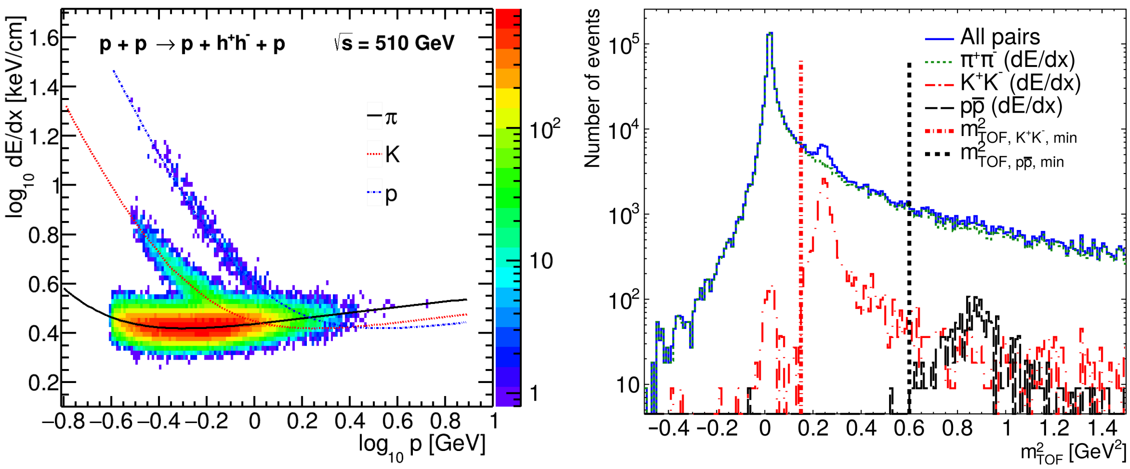

Figure 6. Left: the energy loss $\langle dE/dx \rangle$ of central charged particles as a function of their momenta for CEP event candidates. Colored curves illustrate expected values for pions, kaons, and protons. Right: distributions of invariant mass squared m^2_{TOF} of pions, kaons, and protons. Particles are identified based solely on $\langle dE/dx \rangle$ information. Applied $m^2_{\mathrm{TOF},KK,\mathrm{min}}$ and $m^2_{\mathrm{TOF},p\bar{p},\mathrm{min}}$ cuts are highlighted by dot-dashed lines.

time. The method assumes that both tracks originate from the same vertex and have the same mass. Hence, they have the same squared mass of the particle, m^2_{TOF}, that can be derived from the measured TOF time difference between particles:

$$t_2 - t_1 = l_2\sqrt{1 + \frac{m^2_{\mathrm{TOF}}}{p_2^2}} - l_1\sqrt{1 + \frac{m^2_{\mathrm{TOF}}}{p_1^2}}, \tag{4.5}$$

where $t_{1,2}$ are the time of the tracks' detection in TOF. $l_{1,2}$ and $p_{1,2}$ denote the track lengths and momenta of the particles, respectively, as determined from their trajectories measured by the TPC.

The m^2_{TOF} distributions of pions, kaons, and protons, identified solely based on $\langle dE/dx \rangle$ information, can be seen in figure 6 (right). Peaks close to each particles' invariant mass squared values are seen. Due to the resolution effects, negative, nonphysical values can be seen.

Particle pairs are identified based on the following hypothesis. First, the $p\bar{p}$ pair hypothesis is checked:

$$(\chi^2_{\langle dE/dx \rangle}(p\bar{p}) < 9) \wedge (m^2_{\mathrm{TOF}} > 0.6\ \mathrm{GeV}^2) \wedge (\chi^2_{\langle dE/dx \rangle}(K^+K^-) > 9) \wedge (\chi^2_{\langle dE/dx \rangle}(\pi^+\pi^-) > 9). \tag{4.6}$$

If the hypothesis is satisfied, the pair is identified as a $p\bar{p}$ pair, and if not, the K^+K^- pair hypothesis is tested:

$$(\chi^2_{\langle dE/dx \rangle}(K^+K^-) < 9) \wedge (m^2_{\mathrm{TOF}} > 0.15\ \mathrm{GeV}^2) \wedge (\chi^2_{\langle dE/dx \rangle}(p\bar{p}) > 9) \wedge (\chi^2_{\langle dE/dx \rangle}(\pi^+\pi^-) > 9). \tag{4.7}$$

If neither $p\bar{p}$ nor K^+K^- pair hypothesis is satisfied, the $\pi^+\pi^-$ pair is assumed and the $\pi^+\pi^-$ pair hypothesis is checked:

$$\chi^2_{\langle dE/dx \rangle}(\pi^+\pi^-) < 12. \tag{4.8}$$

This PID technique is designed to minimize misidentification of $\pi^+\pi^-$ pairs as K^+K^- or $p\bar{p}$ pairs. In addition, the PID is restricted to a fiducial acceptance with high track reconstruction efficiency and high pair identification efficiency. The misidentified pairs form a negligible exclusive background ($< 1\%$), as discussed in section 5. The fiducial acceptance of the central hadronic state is defined as:

$$p_{\mathrm{T}}(\pi) > 0.25\ \mathrm{GeV}, \tag{4.9}$$

$$(p_{\mathrm{T}}(K) > 0.3\ \mathrm{GeV}) \wedge (\min(p_{\mathrm{T}}(K^+), p_{\mathrm{T}}(K^-)) < 0.7\ \mathrm{GeV}), \tag{4.10}$$

$$(p_{\mathrm{T}}(p) > 0.4\ \mathrm{GeV}) \wedge (\min(p_{\mathrm{T}}(p), p_{\mathrm{T}}(\bar{p})) < 1.1\ \mathrm{GeV}). \tag{4.11}$$

After all the above selection cuts, there are 86008 $\pi^+\pi^-$, 2454 K^+K^-, and 225 $p\bar{p}$ CEP events.

5 Background estimation

In this section, sources of backgrounds and their quantitative determination are discussed. There are two main sources of background: an exclusive and a non-exclusive background.

The exclusive background comes primarily from incorrectly identified particles species. Namely, when the event passes all the selection criteria but is misidentified due to the incorrectly identified particle species. The dominant contribution to this background comes from $\pi^+\pi^-$ pairs misidentified as K^+K^- or $p\bar{p}$ pairs. The phase space of the measurement is limited to preserve high pair identification efficiency and low probability of misidentification. This background is estimated to be $< 1\%$, and therefore negligible.

The non-exclusive background is the dominant source of background. It arises from non-exclusive events that imitate the h^+h^- topology of CEP: two forward protons, two opposite sign central tracks and large rapidity gaps. The most common sources of the non-exclusive background are:

1. **Accidental coincidences (pile-up):** there can be accidental coincidences of the forward and central system. For example, the overlap of elastic scattering with another inelastic interaction in the central system can imitate a CEP event. Or, it can also be an overlap of a single diffraction event with a proton from the beam halo.

2. **Central Diffraction:** for example, a CEP event with a higher number of produced particles, where only two are detected.

The non-exclusive background subtraction is carried out using missing transverse momentum, (4.3). The method described here is for the invariant mass of $\pi^+\pi^-$, $m(\pi^+\pi^-)$, but the same procedure is applied to all other observables studied in this analysis.

1. The amount of non-exclusive background is estimated in two steps. First, the $p_{\mathrm{T}}^{\mathrm{miss}}$ distribution (see figure 5) is fitted in the sideband region with a second-degree polynomial with the constant term fixed to zero. Second, the fit is extrapolated into the signal region to obtain the amount of background.

2. The $m(\pi^+\pi^-)$ distribution is taken from $p_{\mathrm{T}}^{\mathrm{miss}}$ in $[160, 220]$ MeV. The range is selected to be next to the signal region. There is an assumption that the shape of the background in the selected range is the same as in the signal region.

3. The obtained background distribution is normalized to the expected background amount determined in the first step.

4. Finally, the normalized background distribution is subtracted separately from the $m(\pi^+\pi^-)$ distribution for each bin of the distribution.

Using this method, the amount of non-exclusive background is found to be $19.4 \pm 0.4\%$ for $\pi^+\pi^-$ pairs, $12.1 \pm 0.8\%$ for K^+K^- pairs, and $43 \pm 5\%$ for $p\bar{p}$ pairs.

6 Corrections

The differential fiducial cross section in every bin of the measured quantity of interest, q, is obtained using the formula (6.1):

$$\frac{d\sigma}{dq}(q) = \frac{1}{\Delta q} \times \frac{N^{\mathrm{w}}(q) - N^{\mathrm{w}}_{\mathrm{bkgd}}(q)}{L^{\mathrm{eff}}_{\mathrm{int}}}, \tag{6.1}$$

where Δq is the width of the bin, $N^{\mathrm{w}}(q)$ and $N^{\mathrm{w}}_{\mathrm{bkgd}}(q)$ are the weighted numbers of observed and background events in the given bin, respectively. The weight (w_i) is calculated as:

$$w_i = \frac{1}{\prod_k \varepsilon_{k,i}}, \tag{6.2}$$

where $\varepsilon_{k,i}$ are individual efficiencies for the given i^{th} event. Hence, the weighted numbers of observed events is calculated as:

$$N^{\text{w}}(q) = \sum_{i\in\text{Events}} w_i. \tag{6.3}$$

The effective integrated luminosity $L_{\text{int}}^{\text{eff}}$ is defined as:

$$L_{\text{int}}^{\text{eff}} = \sum_{\text{run}} L_{\text{int}}^{\text{run}} \times P_{\text{retain}}^{\text{CEP}}(\langle L_{\text{inst}}^{\text{run}}\rangle), \tag{6.4}$$

where $L_{\text{int}}^{\text{run}}$ is the integrated luminosity for the given run and $P_{\text{retain}}^{\text{CEP}}(\langle L_{\text{inst}}^{\text{run}}\rangle)$ is the probability of retaining the CEP event as a function of the average instantaneous luminosity ($\langle L_{\text{inst}}^{\text{run}}\rangle$).

6.1 Trigger and luminosity corrections

The integrated luminosity is 121 ± 6 pb^{-1}. It has to be corrected to account for the probability of retaining CEP events, which depends on the instantaneous luminosity. There is a high probability that an exclusive event overlaps with another process and is therefore rejected. This occurs because the CEP trigger includes vetoes ensuring the characteristic double-gap rapidity topology of CEP events. The probability of retaining CEP events is calculated using zero-bias data, taking into account both online and offline vetoes. The online vetoes were part of the trigger definition as described in section 3. The offline veto comes from the requirement of one reconstructed primary TOF vertex. The probability is studied separately for each run[3] and is fitted with an exponential function of the instantaneous luminosity. This reflects the expected Poisson-like behavior of the probability that no interaction occurs in a bunch crossing. The probability of retaining the CEP event is found to be independent of the choice of the RP branch combination. The values of $P_{\text{retain}}^{\text{CEP}}(\langle L_{\text{inst}}^{\text{run}}\rangle)$ vary between $15 - 40\%$, which leads to the effective integrated luminosity of $L_{\text{int}}^{\text{eff}} = 25.6 \pm 1.6$ pb^{-1}.

6.2 TPC and TOF corrections

To determine the TPC and TOF detector efficiencies, an embedding technique is used to simulate the data taking environment. First, Monte Carlo (MC) generated particles are processed using a GEANT3 [28] detector simulation implementing STAR geometry. Second, the output, which mimics raw data from collisions, is superimposed on zero-bias data representing an underlying event.

The TPC track acceptance, reconstruction, and selection efficiencies are studied together and they are used as a TPC efficiency. This efficiency is calculated by tracking how many MC particles are properly reconstructed from the embedded sample. The corrections are calculated as function of $(p_{\mathrm{T}}, \eta, z_{\text{vtx}})$. The typical TPC efficiencies for single hadron are 83% for $\pi^{\pm}$, 63% for $K^{\pm}$, and 78% for p and $\bar{p}$. The typical statistical uncertainties on

[3] A run at STAR refers to a dataset collected during a specific time interval when data was recorded; this typically lies between 30 minutes and 2 hours.

those values are $< 1\%$. The efficiencies for kaons are lower due to weak decays of kaons in front of, or inside, the TPC.

The TOF acceptance, hit reconstruction and TPC track matching to a TOF hit efficiencies are studied together as a TOF efficiency. The efficiency is determined from embedding and compared with a data-driven tag-and-probe method based on decays of K^0_S to $\pi^+\pi^-$. This K^0_S decay channel is selected as it is well established and provides a narrow invariant mass peak clearly separated from the background. The tagged particle is measured by the TPC and the TOF detectors, whereas the probed particle is measured by the TPC and is under study in the TOF. The TOF efficiency for the probed track $\epsilon^{\text{probe}}_{\text{TOF}}$ is calculated as the ratio of two different yields of $\pi^+\pi^-$ pairs satisfying criteria for K^0_S candidates:

$$\epsilon^{\text{probe}}_{\text{TOF}} = \frac{N^{\text{both}}_{\text{TOF}}}{N^{\text{tag}}_{\text{TOF}}}, \tag{6.5}$$

where $N^{\text{both}}_{\text{TOF}}$ and $N^{\text{tag}}_{\text{TOF}}$ are the yields of K^0_S candidates where both pion tracks have TOF hits and where only the tagged pion track is matched to the TOF, respectively. The typical TOF efficiencies are 63% for $\pi^\pm$, 60% for $K^\pm$, and 59% for p and $\overline{p}$.

6.3 PID corrections

The PID efficiency is defined as the probability that the hadron (h^+h^-) pair passes the corresponding pair selection criteria discussed in section 4.5. The same embedded samples that are used for TPC and TOF detector efficiencies are used to determine the PID efficiencies. These are studied as a function of the maximum and minimum true transverse momenta of particles in the pair $(p^{\text{max}}_{\text{T}}, p^{\text{min}}_{\text{T}})$. The efficiency is applied as a function of the $(p^{\text{max}}_{\text{T}}, p^{\text{min}}_{\text{T}})$. The average PID efficiency for $\pi^+\pi^-$ pairs is higher than 99%. At higher values of $p^{\text{min}}_{\text{T}}$, the efficiencies for K^+K^- and $p\overline{p}$ drop significantly due to the requirement of $\chi^2_{\langle dE/dx\rangle}(\pi^+\pi^-) > 9$, which is used to limit misidentification of $\pi^+\pi^-$ pairs in the K^+K^- and $p\overline{p}$ samples. The typical efficiencies for K^+K^- and $p\overline{p}$ pairs are 93% and 95%, respectively.

6.4 Vertex corrections

The criterion on the TPC z-vertex position, discussed in section 4.2, reduces the accepted luminosity relative to the luminosity delivered by the collider. In order to account for this loss, z-positions of primary vertices for each RHIC fill are independently fitted by a normal distribution. Then, the efficiency is estimated based on the obtained values of the mean and standard deviation. Another method is also used. This involves calculating the fraction of lost luminosity directly from the z_{vtx} distribution. The difference between the two methods is about 2% and is independent of the fill number. Therefore, the average of the two efficiency corrections is used to correct the data. A typical vertex-cut efficiency is 90%.

The TPC vertex efficiency is studied using global tracks, which are tracks that are not required to be associated with the primary vertex. Events that mimic CEP are examined to determine if they form a good primary vertex. These events are required to have exactly two good-quality, global TPC tracks matched with TOF. The same good-quality track criteria as described in section 4.3 are applied. The efficiency is determined as follows:

$$\epsilon_{\text{vertex}} = \frac{N^{\text{reco}}_{\text{vertices}}}{N^{\text{examined}}_{\text{vertices}}}, \tag{6.6}$$

where $N^{\text{reco}}_{\text{vertices}}$ and $N^{\text{examined}}_{\text{vertices}}$ are the number of successfully reconstructed and examined vertices, respectively. The average TPC vertex reconstruction efficiency is 89.6%.

6.5 Exclusivity cut corrections

A small fraction of CEP events is lost due to the exclusivity criterion, $p_{\mathrm{T}}^{\text{miss}} < 120$ MeV. The efficiency of the exclusivity criterion is determined as the relative amount of CEP events below the exclusivity criterion from data and MC samples. An MC technique is used to describe the $p_{\mathrm{T}}^{\text{miss}}$ distribution. The MC sample is generated in p_x^{miss} and p_y^{miss} missing space based on the parameters of the fits on p_x^{miss} and p_y^{miss} from the data. The average efficiency from the data and MC is used with typical value above 99%.

6.6 RP corrections

In order to calculate the RP acceptance and track reconstruction and selection efficiency, a dedicated tool (*ppSim*) based on GEANT4 [29] is developed to simulate the response of the RP detectors, as described in Refs. [25, 26]. It includes full implementation of the beamline elements. It also accounts for the background contribution from scattered protons interacting with the material in front of the RPs, and inoperable SVX readout chips [26]. In order to fully reproduce the collision environment, a single proton is generated with total energy of 254.9 GeV. The proton momentum is smeared by the beam angular divergence and propagated through the beamline to the RPs. The *ppSim* output is embedded in the zero-bias events.

There are two parts to the RP efficiency: the detector efficiency and the proton selection efficiency. The detector efficiency for a given branch describes the probability that a proton is measured and reconstructed in that branch. It is calculated as the probability that a single good-quality RP track is reconstructed in the branch. This track must be matched with a true-level primary forward proton. The typical RP detector efficiency is about 98%. That efficiency is compared with a data-driven method, which is based on reconstruction of elastic events. The efficiencies agree within 2σ of statistical uncertainties. The proton selection efficiency reflects the probability that the reconstructed proton will be selected by the reconstruction algorithm. Any additional background from pile-up or noise will lower the proton selection efficiency. The typical value of the RP efficiency for a given branch is about 88%.

Efficiencies quoted above have statistical uncertainties at a fraction of a percent level. Hence, they are negligible compared to the statistical uncertainties of the results. Therefore, they are neither quoted nor propagated.

7 Systematic uncertainties

In this section, we describe how systematic uncertainties are obtained. We find that only the background subtraction systematic uncertainty is bin dependent for all presented results. All other systematic uncertainties are not bin dependent. The following systematic uncertainties are evaluated for each presented distribution separately:

1. **Background subtraction:** the systematic uncertainty related to the non-exclusive background subtraction is discussed in figure 5. It is studied by varying the range of the projection: from 170 to 210 MeV (smaller range) and from 140 to 250 MeV (wider range). The subtraction is performed for the ranges described previously. The obtained fiducial differential cross sections for CEP of h^+h^- pairs as a function $m(h^+h^-)$ are compared with the nominal one. The uncertainty is taken as the average of absolute deviations for each bin separately. There is another source of the systematic uncertainty, which is due to the statistical uncertainty of the size of the non-exclusive background sample. This uncertainty is common for all the bins. The weighted mean of uncertainties of the background subtraction in the invariant mass distribution of $\pi^+\pi^-$, K^+K^-, and $p\bar{p}$ pairs are 0.4%, 0.8%, and 3.3%, respectively. Only this systematic uncertainty is bin dependent for all presented results.

2. **RP efficiency correction:** the systematic uncertainty associated with the RP efficiency corrections for a single proton is studied from run-by-run variations in each RP branch separately. An average variation is approximately 1.5% for a single proton, resulting in the total RP systematic uncertainty on the fiducial differential cross sections being 2.4%.

3. **TPC efficiency correction:** the uncertainty is studied by varying the TPC track selection criteria ($N^{\text{fit}}_{\text{hits}}$ and $N^{\langle dE/dx \rangle}_{\text{hits}}$) and applying the TPC efficiency corrections corresponding to the given set of selection criteria. The obtained fiducial differential cross sections are compared with the cross section calculated with corrections as described in figure 6. The typical uncertainties on the fiducial differential cross sections are $^{+7}_{-4}$%, $^{+7}_{-4}$%, and $^{+4}_{-4}$% for $\pi^+\pi^-$, K^+K^-, and $p\bar{p}$ pairs, respectively.

4. **TOF efficiency correction:** the uncertainty is studied by comparing the corrections obtained from the embedding and the data-driven tag-and-probe method based on $K^0_S \to \pi^+\pi^-$ decays. The difference between the embedding and the tag-and-probe method is found to be about 1.0% per single track. In addition, the corrections from the embedding are calculated as a function of $(p_{\mathrm{T}}, \eta, z_{\text{vtx}})$ with a different binning applied. The obtained fiducial differential cross sections are compared with the cross section calculated with corrections as described in section 6. This method of applying the TOF matching efficiency corrections allows to estimate the related source of uncertainty. The typical total TOF uncertainty on the fiducial differential cross sections is $^{+1}_{-2}$% for $\pi^+\pi^-$, K^+K^-, and $p\bar{p}$ pairs.

5. **TPC vertex reconstruction:** the systematic uncertainty is determined by varying the good primary vertex criteria (DCA_{xy} and DCA_z) and applying the TPC vertex

reconstruction efficiency corrections corresponding to the given set of vertex criteria. The uncertainty on the fiducial differential cross section is $^{+2.6}_{-1.0}$%.

6. **TPC z-vertex criterion:** the uncertainty is calculated as half of the difference between the two methods used as discussed in section 6.4. The systematic uncertainty is determined to be independent of the fill and is 1.1%.

7. **Exclusivity $p_{\mathrm{T}}^{\mathrm{miss}}$ cut:** the systematic uncertainty is 0.4% obtained as the difference between efficiencies obtained using two different methods discussed in section 6.5.

8. **Particle identification:** the uncertainty is studied by varying the pair identification criteria. A typical change of $< 1\%$, $^{+4}_{-5}\%$ and $^{+4}_{-5}\%$ in the fiducial differential cross section is observed for $\pi^+\pi^-$, K^+K^-, and $p\bar{p}$ pairs, respectively. This change results from applying looser and tighter identification criteria and correcting for the corresponding PID efficiency. The looser (tighter) condition replace the value of 9 by 12 (7) in (4.6) and in (4.7) and the value of 12 by 15 (9) in (4.8). The values for the cuts m^2_{TOF} are 0.1 (0.2) and 0.55 (0.7) GeV^2 for the kaon and proton hypotheses, respectively.

9. **The luminosity uncertainty**. There are two parts of the luminosity uncertainty: luminosity calibration based on van der Meer scans [30] and the probability of retaining a CEP event, dependent on instantaneous luminosity. The first of these, contributes to the integrated luminosity uncertainty and is found to be 5% [31]. The second of these, is evaluated to be 4%. Thus, the total uncertainty on effective integrated luminosity (6.4) is 6.4%. This systematic vertical scale uncertainty is not plotted in figures 7–13.

Systematic uncertainties for the integrated fiducial cross sections for CEP of $\pi^+\pi^-$, K^+K^-, and $p\bar{p}$ pairs are shown in figure 2.

	$\delta_{\mathrm{syst}}/\sigma_{\mathrm{fid}}$ [%]				
Particle species	TPC	TOF	RP	Other	Total
$\pi^+\pi^-$	$^{+7}_{-4}$	$^{+1}_{-2}$	2.4	$^{+3}_{-2}$	$^{+8}_{-5}$
K^+K^-	$^{+7}_{-4}$	$^{+1}_{-2}$	2.4	$^{+5}_{-4}$	$^{+9}_{-7}$
$p\bar{p}$	$^{+4}_{-4}$	$^{+1}_{-2}$	2.4	$^{+5}_{-4}$	$^{+7}_{-6}$

Table 2. Systematic uncertainties for the integrated fiducial cross section for CEP of $\pi^+\pi^-$, K^+K^-, and $p\bar{p}$ pairs. The numbers represent the relative systematic uncertainty of the integrated fiducial cross section in percentage.

8 Results

In this section, the results on differential fiducial cross sections and the integrated fiducial cross sections are presented. The fiducial volume of the measurement is common for all the presented results and it is defined in (4.1) for the protons in the RPs, and depending the specific central hadronic state in (4.2), and (4.9)–(4.11).

8.1 Differential fiducial cross sections

In this section, differential fiducial cross sections are presented and compared with predictions from GRANIITTI [32], an MC event generator designed for high energy diffraction with focus on the CEP. It combines up-to-date phenomenological models and approaches [7, 8, 33]. GRANIITTI is the only model that includes a full parametric resonant spectrum, and continuum production with significant interference effects between them. In this analysis, the newest version of GRANIITTI v. 1.090 is compared with our results. That version was tuned to the latest STAR CEP results at $\sqrt{s} = 200$ GeV [3, 34] and is in good agreement with those published results.

Figure 7 shows the differential fiducial cross sections for CEP of $\pi^+\pi^-$, K^+K^-, and $p\bar{p}$ pairs as a function of the difference between azimuthal angles of the forward protons $\Delta\varphi$. In this measurement, the $\Delta\varphi$ is the analogy to the δp_T filter [35], where δp_T is the difference in the transverse momenta of the forward protons. The filter suggests a different $\mathbb{P}$omeron dynamics in different δp_T. Hence, it can filter different quark - antiquark states from glueballs. Strong suppression close to $\Delta\varphi = 90^\circ$ is due to the limited azimuthal acceptance in the RP detector system. However, the same suppression is expected as was seen in CMS and TOTEM [4], where it was attributed to the additional $\mathbb{P}$omeron exchanges between the incoming protons. The acceptance naturally divides the phase space into two ranges of $\Delta\varphi$, where different $\mathbb{P}$omeron dynamics and absorption effects are expected. Therefore, GRANIITTI predictions were produced separately for each $\Delta\varphi$ region: $\Delta\varphi > 90^\circ$ and $\Delta\varphi < 90^\circ$.

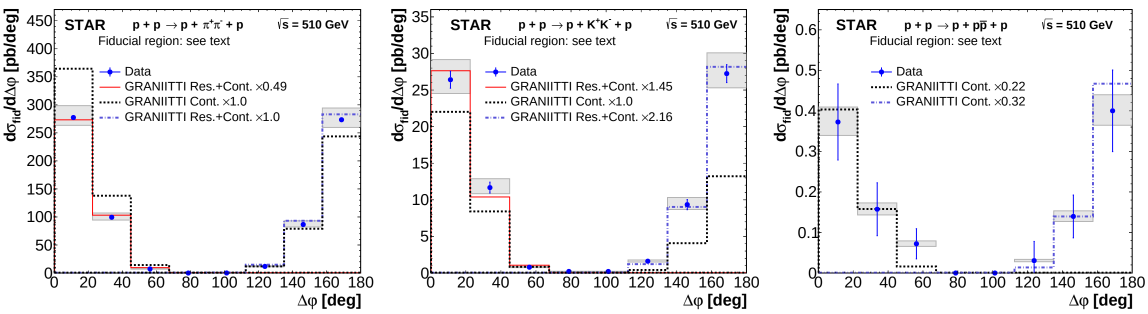

Figure 7. Differential fiducial cross sections of $\pi^+\pi^-$ (left), K^+K^- (middle) and $p\bar{p}$ (right) pairs as a function $\Delta\varphi$ of the forward scattered protons measured in the fiducial volume explained in the text. Data are shown as solid blue points with error bars representing the statistical uncertainties. The systematic uncertainties are shown as gray boxes. The scale uncertainty on the vertical axis due to the effective integrated luminosity is 6.4% and is not shown. Predictions from MC model GRANIITTI [32] are shown separately for each $\Delta\varphi$ region along with the normalization factor.

GRANIITTI predictions are calculated including both continuum (Cont.) and resonance (Res.) contributions. The resonances used in the model are summarized in table 3. This is a minimum set of resonance giving the best description of the data without additional tuning. Subsequently, the predictions are scaled to match the integrated cross section in each $\Delta\varphi$ region. If the scaling factor is within 10% of unity, then no scaling is applied, and factor $\times 1.0$ is used in the legend. The scaling is done only for plotting purposes. Since GRANIITTI is in good agreement with results at $\sqrt{s} = 200$ GeV [3, 34], there is a need for additional tuning of GRANIITTI using results presented here. This may be needed because the two data sets are at different energies and t-ranges, hence two different fiducial regions of the phase space. Moreover, the pure continuum is shown without scaling applied for $\pi^+\pi^-$ and K^+K^- pairs and with scaling for $p\bar{p}$ pairs. The hadron pairs are smeared based on the p_T resolution and the same fiducial criteria for forward protons and central hadrons as described in section 4 are applied.

Particle species	$\Delta\varphi < 90°$ and $\Delta\varphi > 90°$
$\pi^+\pi^-$	$f_0(980)$, $f_2(1270)$, and $f_0(1710)$
K^+K^-	$f_0(980)$, $f_0(1500)$, $f_2(1525)$, and $f_0(1710)$
$p\bar{p}$	only continuum

Table 3. The summary of resonances used in the calculation of GRANIITTI [32] predictions for CEP of $\pi^+\pi^-$, K^+K^-, and $p\bar{p}$ pairs in two regions of the difference in azimuthal angles $\Delta\varphi$ of the forward scattered protons: $\Delta\varphi > 90°$ and $\Delta\varphi < 90°$.

Figure 8 shows differential fiducial cross sections of $\pi^+\pi^-$, K^+K^-, and $p\bar{p}$ pairs as a function of the invariant mass of the pair in two $\Delta\varphi$ regions measured within the STAR acceptance in proton-proton collisions at $\sqrt{s} = 510$ GeV. GRANIITTI predictions are shown as well with the same scaling as in figure 7.

In the $\pi^+\pi^-$ invariant mass distribution in both $\Delta\varphi$ regions, expected features seen in previous CEP [2–4] and central production [6] measurements are observed: a sharp drop at about 1 GeV attributed to the quantum mechanical negative interference of $f_0(980)$ with the continuum contribution, and a peak consistent with the $f_2(1270)$. A clear difference between the two $\Delta\varphi$ regions can be seen. In $\Delta\varphi < 90°$, an enhancement at low invariant mass and a suppression the region of $f_2(1270)$ resonance are observed. The enhancement is mainly due to the kinematics of the forward protons at $\Delta\phi < 90°$ as it opens an acceptance compared to the $\Delta\phi > 90°$. Above $m(\pi^+\pi^-) > 1.5$ GeV, there are no significant structures in the cross section, which generally decreases with increasing invariant mass. Evidence of structures at 1.7 and 1.9 GeV in $\Delta\varphi > 90°$ can be seen. The first one can be attributed to the $f_0(1710)$ resonance that was considered as a "pure" glueball candidate [36]. Moreover, there is no peak around the mass $m(\pi^+\pi^-) \sim 0.8$ GeV that could be attributed to the $\rho(770)$ meson. Hence, the contributions from photoproduction and Reggeon exchanges should be insignificant as it is expected at RHIC energies. The observed spectrum is consistent with DIPE.

Although GRANIITTI had to be scaled to match the data, the spectrum with its main features is described quite well. There are few differences: the higher cross section above $m(\pi^+\pi^-) > 1.5$ GeV in $\Delta\varphi > 90°$ and the more pronounced $f_0(980)$ resonance in $\Delta\varphi < 90°$. Also, the enhancement in the invariant mass at about 500 MeV could be attributed to the $f_0(500)$ resonance. However, that contribution to the mass spectrum would have to be tuned in GRANIITTI.

In the invariant mass of K^+K^- pairs, a strong dependence of differential fiducial cross sections on the azimuthal separation between forward protons ($\Delta\varphi < 90°, \Delta\varphi > 90°$) is

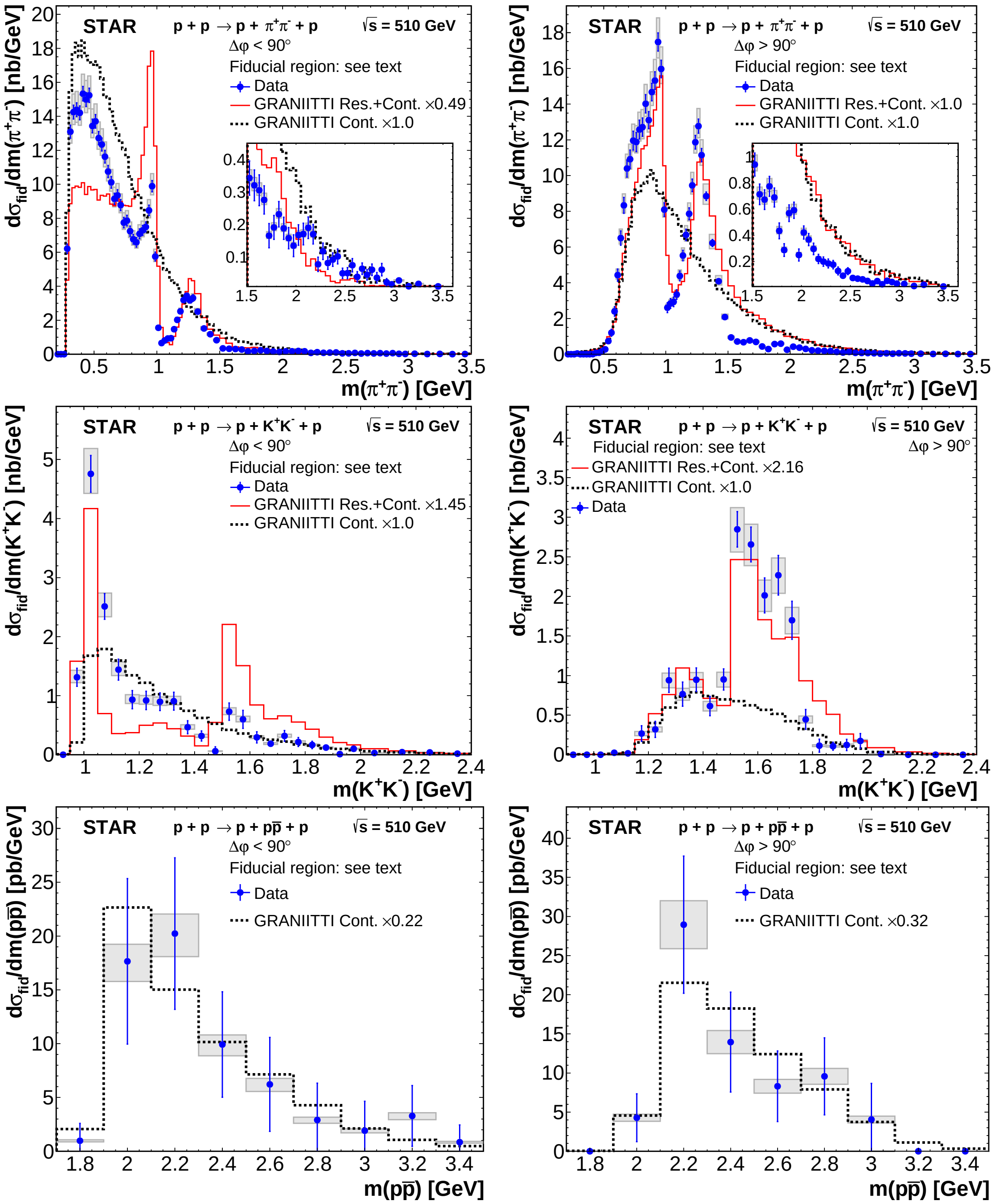

Figure 8. Differential fiducial cross sections of $\pi^+\pi^-$ (top), K^+K^- (middle), and $p\bar{p}$ (bottom) pairs as a function of the invariant mass of the pair in two regions of the difference in azimuthal angles $\Delta\varphi$ of the forward scattered protons: $\Delta\varphi < 90°$ (left) and $\Delta\varphi > 90°$ (right), measured in the fiducial volume explained in the text. Data are shown as solid blue points with error bars representing the statistical uncertainties. The systematic uncertainties are shown as gray boxes. The scale uncertainty on the vertical axis due to the effective integrated luminosity is 6.4% and is not shown. Predictions from MC model GRANIITTI [32] are shown separately for each $\Delta\varphi$ region along with the normalization factor.

observed. In particular, there is a strong enhancement at low invariant mass in $\Delta\varphi < 90°$. Based on the comparison with GRANIITTI, the enhancement is attributed solely to the $f_0(980)$ resonance contribution.

This is the first observation of $f_0(980)$ production in the K^+K^- channel. This is because the experimental setup allows for the detection of states close to the production threshold, particularly in the region of large transverse momentum. The next possible resonance would be $\varphi(1020)$ meson produced via the photoproduction process. However, the contribution from this process is not significant, as in the earlier discussion that photoproduction and Reggeon exchanges are not significant in the $\pi^+\pi^-$ channel.

For $\Delta\varphi > 90°$, two structures are seen at about 1.3 and 1.5 GeV. In GRANIITTI, the broad structure around 1.3 GeV is due to the acceptance cut off of the K^+K^- continuum invariant mass distribution at the lower masses, while the peak at $\sim$ 1.5 GeV can be explained by $f_0(1500)$ and $f_2(1525)$. There is also a possible peak at $\sim$ 1.7 GeV, which could be due to the $f_0(1710)$ resonance. Also a possible enhancement at $m(K^+K^-) \sim 1.975$ GeV is seen.

For $\Delta\varphi < 90°$, peaks at 1 GeV and 1.5 GeV are seen. They correspond to $f_0(980)$ and ($f_0(1500)$, $f_2(1525)$) resonances. Also, a dip is observed at $m(K^+K^-) \lesssim 1.5$ GeV. The dip can be explained as due to the negative interference of $f_0(1500)$ with the continuum production. Also, an enhancement corresponding to $f_0(1710)$ is seen.

Data do not support the presence of the $f_2(1270)$ resonance and GRANIITTI reproduces the invariant mass spectrum quite well without the $f_2(1270)$.

The differential fiducial cross sections of $p\bar{p}$ pairs do not show any significant resonances or any notable $\Delta\varphi$ asymmetry. Hence, it is compared with the GRANIITTI predictions based solely on continuum contributions. An enhancement at the level of 1σ at $m(p\bar{p}) \sim$ 2.2 GeV for $\Delta\varphi > 90°$ is seen. It was also observed at the same level at $\sqrt{s} = 200$ GeV [3].

Figure 9 shows differential fiducial cross sections of $\pi^+\pi^-$, K^+K^-, and $p\bar{p}$ pairs as a function of the pair rapidity in two $\Delta\varphi$ regions. The GRANIITTI predictions are shown as well with the same scaling as in figure 7. In general, the shapes of the measured distributions are well described by the GRANIITTI predictions and show the same behavior as at $\sqrt{s} = 200$ GeV [3].

Figure 10 shows differential fiducial cross sections of $\pi^+\pi^-$, K^+K^-, and $p\bar{p}$ pairs as a function of the absolute value of the sum of the squares of the four-momentum transfer of the forward protons ($|t_1 + t_2|$) in two $\Delta\varphi$ regions. GRANIITTI predictions are shown as well. The same scaling as in the invariant mass distributions is applied. The shapes of the measured distributions are strongly affected by the fiducial cuts applied to the forward scattered protons. In general, the shapes are well described by the GRANIITTI predictions in $\Delta\varphi < 90°$ while the distributions in $\Delta\varphi > 90°$ are slightly shifted to the higher values in the model. The shapes are similar to those observed at $\sqrt{s} = 200$ GeV [3].

The large statistics of the $\pi^+\pi^-$ sample enables a more detailed study. The differential fiducial cross sections are studied in three characteristic ranges of the invariant mass of the pair: $m(\pi^+\pi^-) < 1$ GeV, 1 GeV $< m(\pi^+\pi^-) < 1.5$ GeV and $m(\pi^+\pi^-) > 1.5$ GeV. The first region is considered to be dominated by continuum production. The second is dominated by resonant production, namely by $f_2(1270)$.

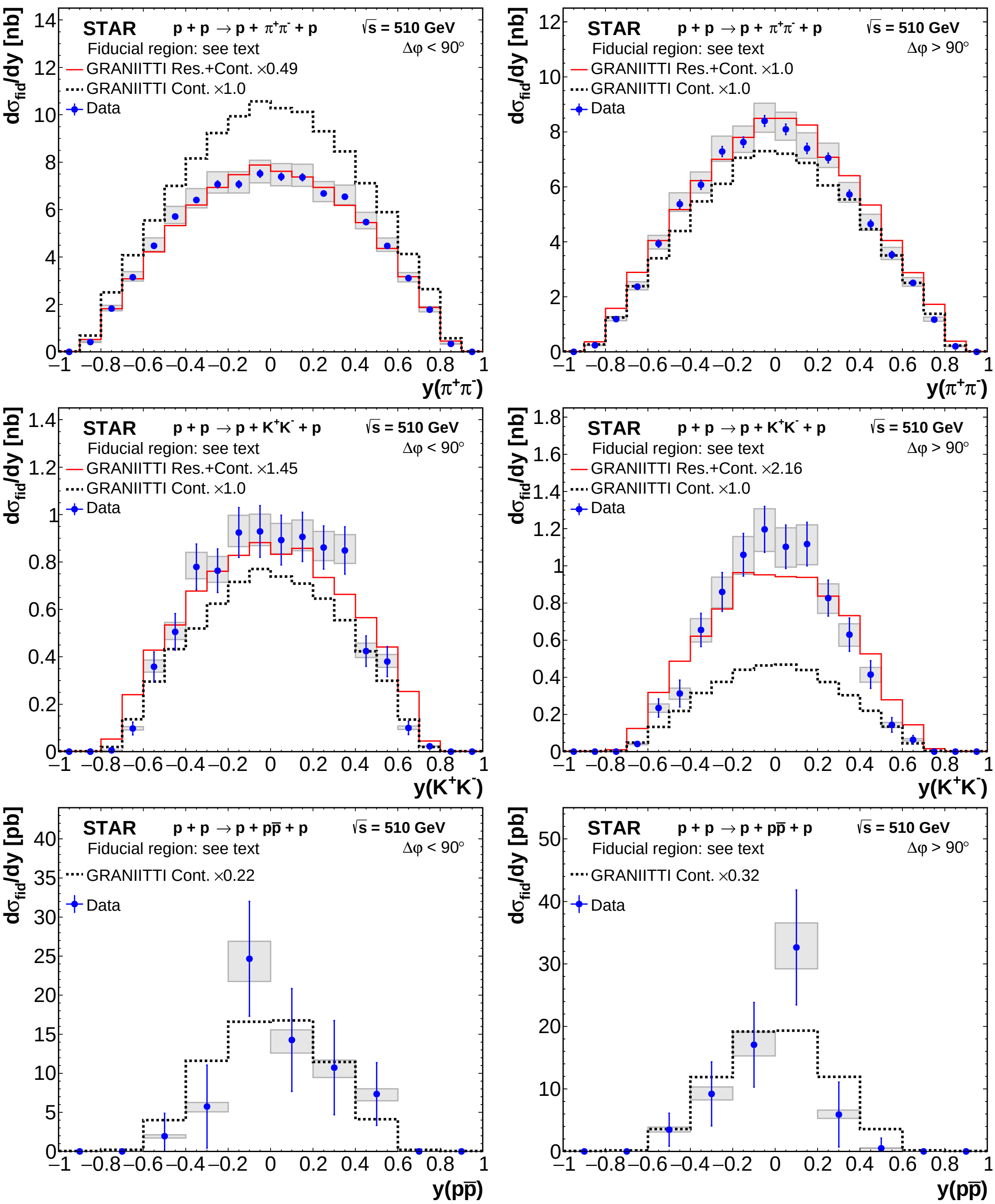

Figure 9. Differential fiducial cross sections of $\pi^+\pi^-$ (top), K^+K^- (middle), and $p\bar{p}$ (bottom) pairs as a function of the pair rapidity in two regions of the difference in azimuthal angles $\Delta\varphi$ of the forward scattered protons: $\Delta\varphi < 90°$ (left) and $\Delta\varphi > 90°$ (right), measured in the fiducial volume explained in the text. Data are shown as solid blue points with error bars representing the statistical uncertainties. The systematic uncertainties are shown as gray boxes. The scale uncertainty on the vertical axis due to the effective integrated luminosity is 6.4% and is not shown. Predictions from MC model GRANIITTI [32] are shown separately for each $\Delta\varphi$ region along with the normalization factor.

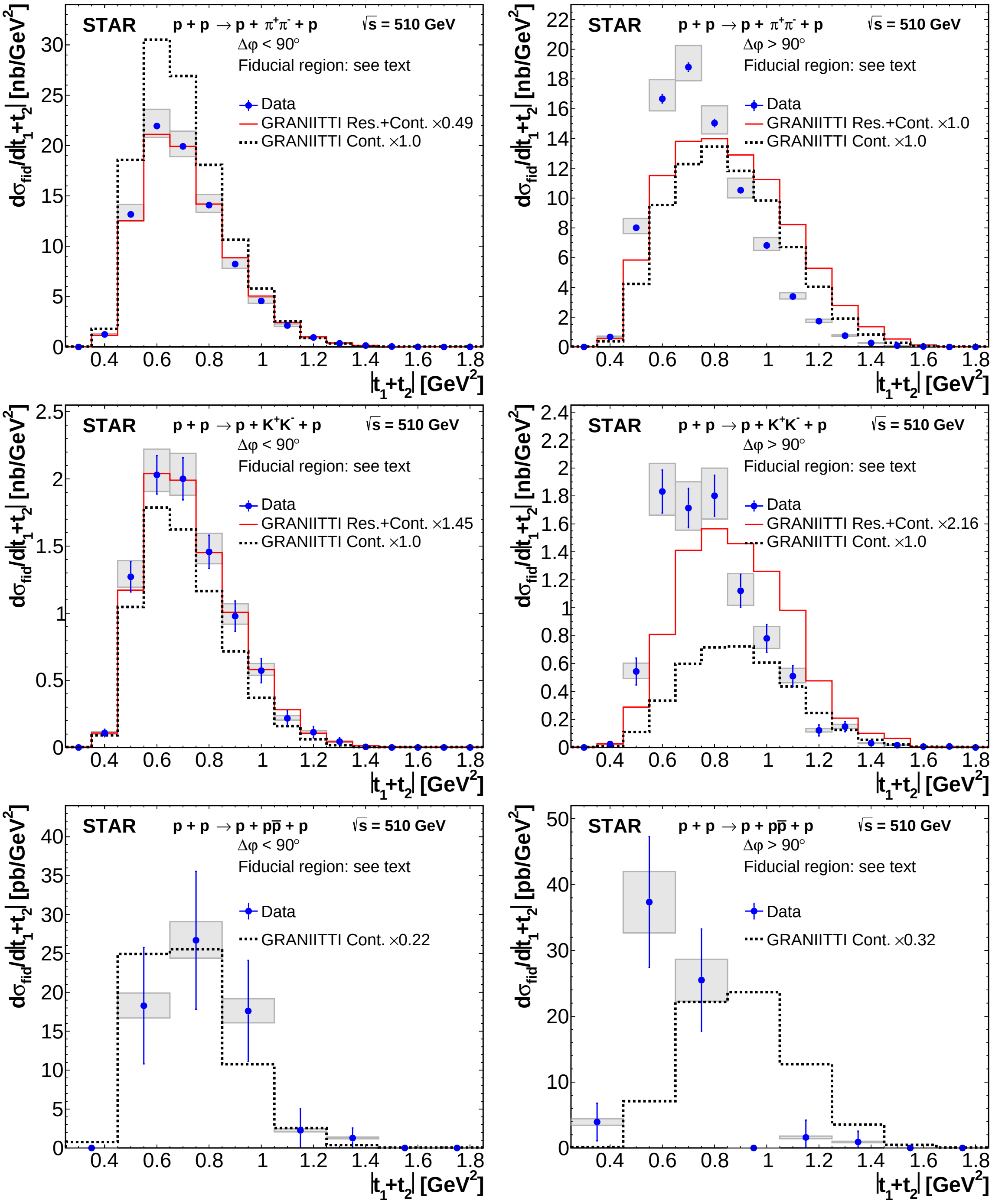

Figure 10. Differential fiducial cross sections for CEP of $\pi^+\pi^-$ (top), K^+K^- (middle), and $p\bar{p}$ (bottom) pairs as a function of the absolute value of the sum of the squares of the four-momentum transfer of the forward protons in two regions of the difference in azimuthal angles $\Delta\varphi$ of the forward scattered protons: $\Delta\varphi < 90°$ (left) and $\Delta\varphi > 90°$ (right), measured in the fiducial volume explained in the text. Data are shown as solid blue points with error bars representing the statistical uncertainties. The systematic uncertainties are shown as gray boxes. The scale uncertainty on the vertical axis due to the effective integrated luminosity is 6.4% and is not shown. Predictions from MC model GRANIITTI [32] are shown separately for each $\Delta\varphi$ region along with the normalization factor.

Figure 11 shows differential fiducial cross sections of $\pi^+\pi^-$ pairs as a function of the difference in azimuthal angles ($\Delta\varphi$) of the forward scattered protons in three ranges of the $\pi^+\pi^-$ pair invariant mass. GRANIITTI predictions are shown as well. The strong suppression close to $\Delta\varphi = 90^\circ$ is due to the limited azimuthal acceptance in the RP detector system. The differential fiducial cross sections in $\Delta\varphi > 90^\circ$ in the first range of the $\pi^+\pi^-$ pair invariant mass is suppressed due to the STAR TPC acceptance. The same suppression was observed also at $\sqrt{s} = 200$ GeV [3]. In the other ranges, suppressions of differential fiducial cross sections in $\Delta\varphi < 90^\circ$ are seen. The suppression in the middle range was also seen at $\sqrt{s} = 200$ GeV [3] and is also predicted by GRANIITTI calculations assuming only the continuum contribution. In the last range, GRANIITTI predicts the same asymmetry as seen in the data.

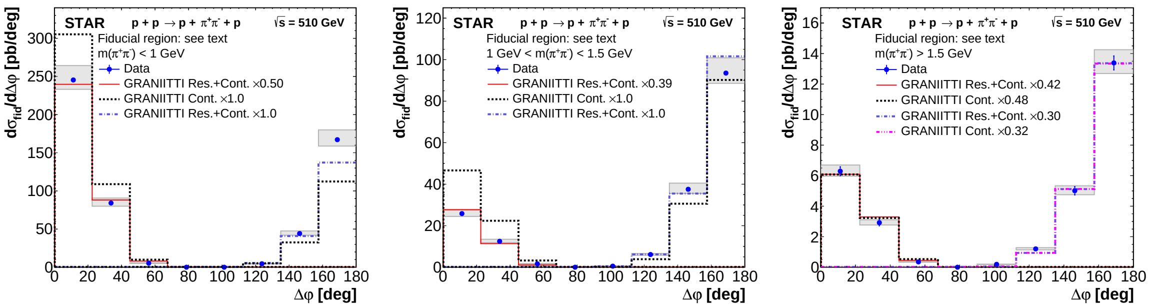

Figure 11. Differential fiducial cross sections of $\pi^+\pi^-$ pairs as a function of the difference in azimuthal angles $\Delta\varphi$ of the forward scattered protons in three ranges of the $\pi^+\pi^-$ pair invariant mass: $m(\pi^+\pi^-) < 1$ GeV (left), 1 GeV $< m(\pi^+\pi^-) < 1.5$ GeV (middle) and $m(\pi^+\pi^-) > 1.5$ GeV (right), measured in the fiducial volume explained in the text. Data are shown as solid blue points with error bars representing the statistical uncertainties. The systematic uncertainties are shown as gray boxes. The scale uncertainty on the vertical axis due to the effective integrated luminosity is 6.4% and is not shown. Predictions from MC model GRANIITTI [32] are shown separately for each $\Delta\varphi$ region along with the normalization factor.

Figure 12 shows differential fiducial cross sections of hadron $\pi^+\pi^-$ pairs as a function of the pair rapidity in three ranges of the $\pi^+\pi^-$ pair invariant mass and in two $\Delta\varphi$ regions. GRANIITTI predictions are shown as well with the same scaling as in figure 11. The GRANIITTI predictions describe well the shapes of measured differential fiducial cross sections in both $\Delta\varphi$ regions and in all three ranges of the $\pi^+\pi^-$ pair invariant mass. The measured shapes are similar to those observed at $\sqrt{s} = 200$ GeV [3].

Figure 13 shows differential fiducial cross sections of $\pi^+\pi^-$ pairs as a function of $|t_1+t_2|$ in three ranges of the $\pi^+\pi^-$ pair invariant mass and in two $\Delta\varphi$ regions. GRANIITTI predictions are shown as well with the same scaling as in figure 11. The GRANIITTI predictions describe well the shapes of measured differential fiducial cross sections in $\Delta\varphi < 90^\circ$ in all three ranges of the $\pi^+\pi^-$ pair invariant mass. In $\Delta\varphi > 90^\circ$, the GRANIITTI prediction reproduces the shape only for the higher invariant masses while the predictions are shifted to the higher values of $|t_1 + t_2|$ for the first two ranges. The measured shapes are comparable to those observed at $\sqrt{s} = 200$ GeV [3]. The higher range of $|t_1 + t_2|$ is due to higher momentum of the forward protons compared to that at $\sqrt{s} = 200$ GeV [3].

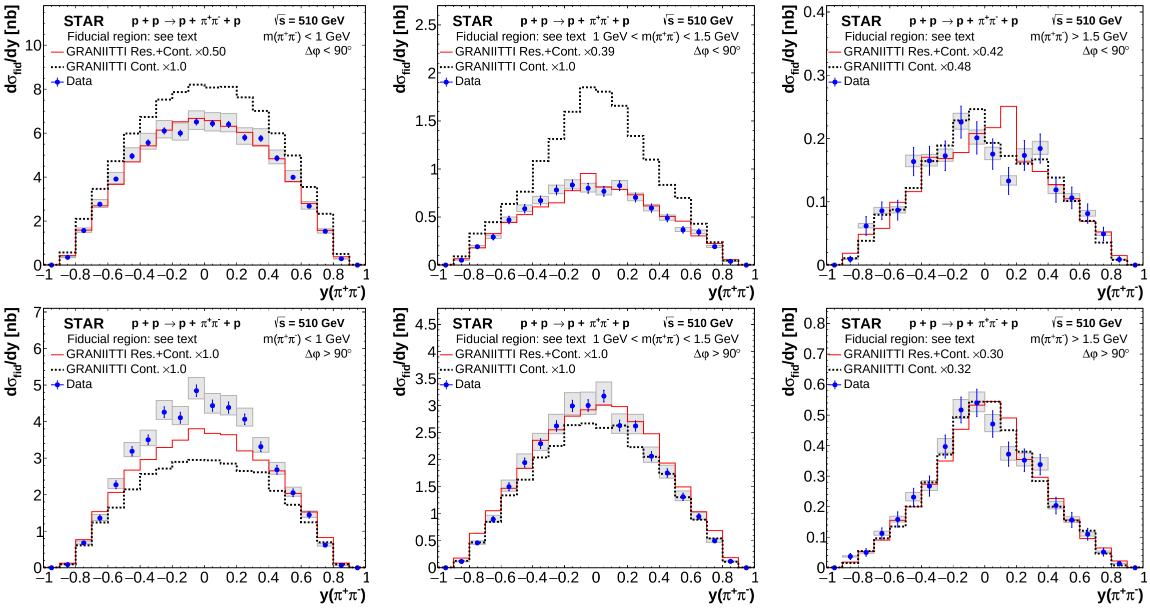

Figure 12. Differential fiducial cross sections of $\pi^+\pi^-$ pairs as a function of the pair rapidity in three ranges of the $\pi^+\pi^-$ pair invariant mass: $m(\pi^+\pi^-) < 1$ GeV (left), 1 GeV $< m(\pi^+\pi^-) < 1.5$ GeV (middle) and $m(\pi^+\pi^-) > 1.5$ GeV (right) and in to two regions of the difference in azimuthal angles $\Delta\varphi$ of the forward scattered protons: $\Delta\varphi < 90°$ (top) and $\Delta\varphi > 90°$ (bottom), measured in the fiducial volume explained in the text. Data are shown as solid blue points with error bars representing the statistical uncertainties. The systematic uncertainties are shown as gray boxes. The scale uncertainty on the vertical axis due to the effective integrated luminosity is 6.4% and is not shown. Predictions from MC model GRANIITTI [32] are shown separately for each $\Delta\varphi$ region along with the normalization factor.

8.2 Integrated fiducial cross sections

In $m(h^+h^-)$, the integrated fiducial cross sections of $\pi^+\pi^-$, K^+K^-, and $p\bar{p}$ pairs, measured in the fiducial volume explained in the text above, are calculated separately for two regions of the difference in azimuthal angles $\Delta\varphi$ of the forward scattered protons: $\Delta\varphi > 90°$ and $\Delta\varphi < 90°$. The results are presented in table 4.

Particle species	Unit	$\sigma_{\text{fid}} \pm \delta_{\text{stat}} \pm \delta_{\text{syst}}$	
		$\Delta\varphi < 90°$	$\Delta\varphi > 90°$
$\pi^+\pi^-$	nb	$8.68 \pm 0.04\ ^{+0.64}_{-0.43}$	$8.42 \pm 0.04\ ^{+0.64}_{-0.41}$
K^+K^-	pb	$879 \pm 27\ ^{+78}_{-57}$	$868 \pm 28\ ^{+81}_{-84}$
$p\bar{p}$	pb	$13.9 \pm 1.4\ ^{+0.8}_{-1.3}$	$14.4 \pm 1.5\ ^{+1.1}_{-1.1}$

Table 4. Integrated fiducial cross sections for CEP of $\pi^+\pi^-$, K^+K^-, and $p\bar{p}$ pairs measured in the fiducial volume explained in the text. Integrated cross sections are presented in to two regions of the difference in azimuthal angles $\Delta\varphi$ of the forward scattered protons: $\Delta\varphi > 90°$ and $\Delta\varphi < 90°$. Statistical and systematic uncertainties are provided for each cross section.

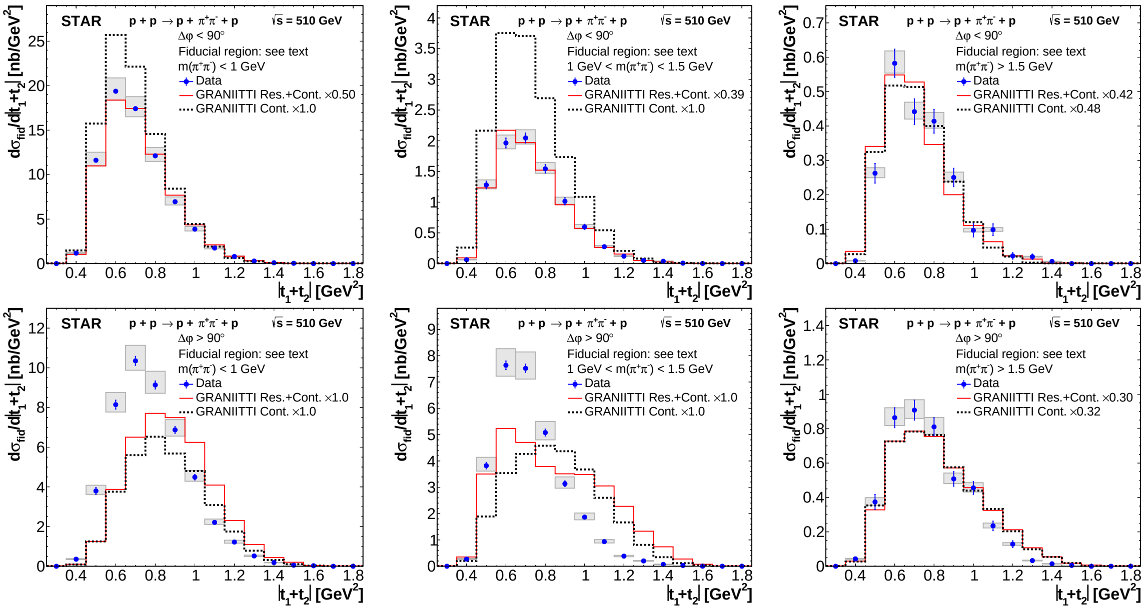

Figure 13. Differential fiducial cross sections of $\pi^+\pi^-$ pairs as a function of the absolute value of the sum of the squares of the four-momentum transfer of the forward protons in three ranges of the $\pi^+\pi^-$ pair invariant mass: $m(\pi^+\pi^-) < 1$ GeV (left), 1 GeV $< m(\pi^+\pi^-) < 1.5$ GeV (middle) and $m(\pi^+\pi^-) > 1.5$ GeV (right) and in to two regions of the difference in azimuthal angles $\Delta\varphi$ of the forward scattered protons: $\Delta\varphi < 90°$ (top) and $\Delta\varphi > 90°$ (bottom), measured in the fiducial volume explained in the text. Data are shown as solid blue points with error bars representing the statistical uncertainties. The systematic uncertainties are shown as gray boxes. The scale uncertainty on the vertical axis due to the effective integrated luminosity is 6.4% and is not shown. Predictions from MC model GRANIITTI [32] are shown separately for each $\Delta\varphi$ region along with the normalization factor.

9 Summary

We present the first results on the CEP of oppositely charged hadron pairs ($\pi^+\pi^-$, K^+K^-, and $p\bar{p}$) in pp collisions at $\sqrt{s} = 510$ GeV using the STAR detector at RHIC. The measurement of forward-scattered protons enabled full control of the process kinematics and verification of its exclusivity. The measurements are presented within the STAR detector's acceptance, which is determined from the transverse momenta and pseudorapidities of the centrally produced charged hadron pairs, as well as the momenta of forward-scattered protons.

The differential fiducial cross sections are presented as functions of the $\Delta\varphi$, $|t_1 + t_2|$, $m(h^+h^-)$, and $y(h^+h^-)$ in two regions of $\Delta\varphi$. Structures observed in the invariant mass spectra of $\pi^+\pi^-$ and K^+K^- pairs suggest that DIPE is the dominant production mechanism in this fiducial phase space. We observe a strong dependence of the cross section measured here, $d\sigma/dm(h^+h^-)$, on $\Delta\varphi$ suggesting different IPomeron interactions in each $\Delta\varphi$ region.

For $\pi^+\pi^-$ pairs, the invariant mass spectrum is consistent with the $f_0(980)$ and $f_2(1270)$ resonances, which have been observed in previous measurements at other collision energies [2–4, 6]. Also, an enhancement consistent with the $f_0(1710)$ is observed.

For K^+K^- pairs, the observed features can be explained as due to the $f_0(980)$, $f_0(1500)$, $f_2(1525)$, and $f_0(1710)$ resonances. Notably, the $f_0(980)$ resonance is observed for the first time in the K^+K^- decay channel, as the experimental setup opened an acceptance of states close to the production threshold at large transverse momentum. The limited statistics do not allow any significant conclusions about the resonances in the $p\bar{p}$ invariant mass spectrum.

We also present the rapidity distributions of the central states and the $|t_1 + t_2|$, and $\Delta\varphi$ distributions of the forward protons. In the $\pi^+\pi^-$ channel, these distributions are present in three mass regions.

We also present a comparison of the results with predictions from GRANIITTI v1.090 event generator, which was tuned to and is in good agreement with the results at $\sqrt{s} = 200$ GeV [3, 34]. In general, GRANIITTI describes the shape of the distributions, but additional scaling factor in the range 0.3 to 1.8 is often needed to match the results. The new data presented here will allow for additional tuning of GRANIITTI and other models of CEP. For example, tuning the contribution from the $f_0(500)$ resonance may improve the agreement between GRANIITTI and the data.

Acknowledgments

We thank the RHIC Operations Group and SDCC at BNL, the NERSC Center at LBNL, and the Open Science Grid consortium for providing resources and support. This work was supported in part by the Office of Nuclear Physics within the U.S. DOE Office of Science, the U.S. National Science Foundation, National Natural Science Foundation of China, Chinese Academy of Science, the Ministry of Science and Technology of China and the Chinese Ministry of Education, NSTC Taipei, the National Research Foundation of Korea, Czech Science Foundation and Ministry of Education, Youth and Sports of the Czech Republic, Hungarian National Research, Development and Innovation Office, New National Excellency Programme of the Hungarian Ministry of Human Capacities, Department of Atomic Energy and Department of Science and Technology of the Government of India, the National Science Centre and WUT ID-UB of Poland, the Ministry of Science, Education and Sports of the Republic of Croatia, German Bundesministerium für Bildung, Wissenschaft, Forschung and Technologie (BMBF), Helmholtz Association, Ministry of Education, Culture, Sports, Science, and Technology (MEXT), and Japan Society for the Promotion of Science (JSPS).

References

[1] V. Barone and E. Predazzi, *High-Energy Particle Diffraction*, Springer, Germany (2002).

[2] Axial Field Spectrometer collaboration, *A search for glueballs and a study of double pomeron exchange at the CERN intersecting storage rings*, Nucl. Phys. B **264** (1986) 154.

[3] STAR collaboration, *Measurement of the central exclusive production of charged particle pairs in proton-proton collisions at $\sqrt{s} = 200$ GeV with the STAR detector at RHIC*, JHEP **2020** (2020) 46.

[4] CMS and TOTEM collaboration, *Nonresonant central exclusive production of charged-hadron pairs in proton-proton collisions at* $\sqrt{s} = 13$ TeV, *Phys. Rev. D* **109** (2024) 112013.

[5] ATLAS collaboration, *Measurement of exclusive pion pair production in proton-proton collisions at* $\sqrt{s} = 7$ *TeV with the ATLAS detector*, *Eur. Phys. J. C* **83** (2023) 627.

[6] CDF collaboration, *Measurement of central exclusive* $\pi^+\pi^-$ *production in* $p\bar{p}$ *collisions at* $\sqrt{s} = 0.9$ *and 1.96 TeV at CDF*, *Phys. Rev. D* **91** (2015) 091101.

[7] L.A. Harland-Lang, V.A. Khoze, M.G. Ryskin and W.J. Stirling, *Central exclusive production within the Durham model: a Review*, *Int. J. Mod. Phys. A* **29** (2014) 1430031.

[8] P. Lebiedowicz, et al., *Central exclusive diffractive production of the* $\pi^+\pi^-$ *continuum, scalar, and tensor resonances in pp and* $p\bar{p}$ *scattering within the tensor Pomeron approach*, *Phys. Rev. D* **93** (2016) 054015.

[9] C. Ewerz, P. Lebiedowicz, O. Nachtmann and A. Szczurek, *Helicity in proton–proton elastic scattering and the spin structure of the pomeron*, *Phys. Lett. B* **763** (2016) 382.

[10] V.A. Khoze, A.D. Martin and M.G. Ryskin, *Multiple interactions and rapidity gap survival*, *J. Phys. G: Nucl. Part. Phys.* **45** (2018) 053002.

[11] P. Lebiedowicz and A. Szczurek, *Revised model of absorption corrections for the* $pp \to pp\pi^+\pi^-$ *process*, *Phys. Rev. D* **92** (2015) 054001.

[12] W. Ochs, *The status of glueballs*, *J. Phys. G* **40** (2013) 043001.

[13] S. Ganguli and D. Roy, *Regge phenomenology of inclusive reactions*, *Physics Reports* **67** (1980) 201.

[14] J.R. Forshaw and D.A. Ross, *Quantum chromodynamics and the pomeron*, Cambridge University Press, New York, 1st ed. (1997).

[15] PP2PP collaboration, *The PP2PP experiment at RHIC: silicon detectors installed in Roman Pots for forward proton detection close to the beam*, *Nucl. Instrum. Meth. A* **535** (2004) 6.

[16] STAR collaboration, *The STAR time projection chamber: a unique tool for studying high multiplicity events at RHIC*, *Nucl. Instrum. Meth. A* **499** (2003) 20.

[17] STAR collaboration, *The large-area time-of-flight (TOF) upgrade for the STAR detector*, *AIP Conf. Proc.* **1099** (2009) 778.

[18] STAR collaboration, *The Beam-Beam Counter: a local polarimeter at STAR*, *AIP Conf. Proc.* **2008** (2008) 390.

[19] M. Harrison, et al., *The RHIC accelerator*, *Annu. Rev. Nucl. Part. Sci.* **52** (2002) 425.

[20] H. Hahn, et al., *The RHIC design overview*, *Nucl. Instrum. Meth. A* **499** (2003) 245.

[21] STAR collaboration, *STAR detector overview*, *Nucl. Instrum. Meth. A* **499** (2003) 624.

[22] W. Llope, et al., *The STAR Vertex Position Detector*, *Nucl. Instrum. Methods Phys. Res. A* **759** (2014) 23.

[23] C. Adler, et al., *The RHIC zero degree calorimeters*, *Nucl. Instrum. Meth. A* **470** (2001) 488.

[24] C. Adler, et al., *The RHIC zero-degree calorimeters*, *Nucl. Instrum. Meth. A* **499** (2003) 433.

[25] STAR collaboration, *Results on total and elastic cross sections in proton–proton collisions at* $\sqrt{s} = 200$ *GeV*, *Phys. Rev. Lett. B* **808** (2020) 135663.

[26] STAR collaboration, *Results on elastic cross sections in proton–proton collisions at $\sqrt{s} = 510$ GeV with the STAR detector at RHIC*, Phys. Rev. Lett. B **852** (2024) 138601.

[27] H. Bichsel, *A method to improve tracking and particle identification in TPCs and silicon detectors*, Nucl. Instrum. Meth. A **562** (2006) 154.

[28] R. Brun, F. Bruyant, M. Maire, A.C. McPherson and P. Zanarini, *GEANT 3*, CERN, Geneva (1987).

[29] GEANT4 collaboration, *GEANT4—a simulation toolkit*, Nucl. Instrum. Methods Phys. Res., Sect. A **506** (2003) 250.

[30] S. van der Meer, *Calibration of the Effective Beam Height in the ISR*, Tech. Rep. CERN-ISR-PO-68-31 (1968).

[31] STAR collaboration, *Measurements of the Z^0/γ^* cross section and transverse single spin asymmetry in 510 GeV p+p collisions*, Phys. Rev. Lett. B **854** (2024) 138715.

[32] M. Mieskolainen, *GRANIITTI: A Monte Carlo Event Generator for High Energy Diffraction*, 1910.06300.

[33] C. Ewerz, M. Maniatis and O. Nachtmann, *A model for soft high-energy scattering*, Ann. Phys. **342** (2014) 31.

[34] M. Mieskolainen, *Graniitti: Towards a Deep Learning-enhanced Monte Carlo Event Generator for High-energy Diffraction*, Acta Phys. Pol. B Proc. Suppl. **16** (2023) 6.

[35] F.E. Close and A. Kirk, *Glueball-qq filter in central hadron production*, Phys. Lett. B **397** (1997) 333.

[36] S. Dobbs, A. Tomaradze, T. Xiao and K.K. Seth, *Comprehensive study of the radiative decays of J/ψ and $\psi(2S)$ to pseudoscalar meson pairs, and search for glueballs*, Phys. Rev. D **91** (2015) 052006.

The STAR Collaboration